Ciência Rural, Santa Maria, v.56:7, e20250457, 2026 http://doi.org/10.1590/0103-8478cr20250457
ISSNe 1678-4596
CROP PRODUCTION

Season-long potato yield prediction from unmanned aerial vehicle multispectral imagery using a hybrid LSTM–XGBoost model under disease stress

Shaofan Tang[1] Yilong Peng[2] Jian Dao[3] Jiaming Xu[1] Ji Gao[1]
Jiani Liu[1] Ying Zhang[1] Fu Wang[1] Jianhua Li[1,4,5,*]

[1]College of Water Conservancy, Yunnan Agricultural University, 650201, Kunming, China.
[2]Faculty of Science, The University of Queensland, St Lucia, Brisbane, QLD 4072, Australia.
[3]Key Laboratory of Plant Pathology, College of Plant Protection, Yunnan Agricultural University, 650201, Kunming, China.
[4]Luliang Mountain Basin Land Use Field Scientific Observation Station of Yunnan Province, 655600, Luliang, Yunnan, China.
[5]Yunnan Mountain Basin Field Science Observation and Research Station, Ministry of Natural Resources of China, 650201, Kunming, China.
E-mail: wenniforever@126.com. *Corresponding author.

ABSTRACT: The potato is a key food and cash crop in China, requiring accurate yield forecasting for precision agriculture and timely disease management. This study was conducted on 54 plots (3.5 m × 8 m) in Yunnan Province, with multispectral imagery collected by UAVs at four phenological stages: bud emergence, early flowering, full bloom, and senescence. A hybrid model combining Long Short-Term Memory (LSTM) networks with Extreme Gradient Boosting (XGBoost) was developed to exploit temporal dynamics and regression capacity. In single-stage evaluations, the model performed best at senescence (R^2 = 0.939, RMSE = 856.4 kg ha^{-1}, MAE = 712.9 kg ha^{-1}), indicating strong correlation between vegetation indices and yield. When integrating all stages, the long-sequence model for healthy plots achieved R^2 = 0.799, RMSE = 1598.4 kg ha^{-1}, and MAE = 1465.9 kg ha^{-1}. Incorporating five severely diseased plots slightly reduced performance (R^2 = 0.738), yet accuracy remained acceptable. To reflect real-world farming conditions, three disease treatments were applied: pathogen-inoculated, pathogen-suppressed with horseradish extract, and natural-disease groups. Across these scenarios, the LSTM-XGBoost consistently outperformed conventional regression models. The results demonstrated that the hybrid approach effectively captures temporal growth dynamics and reduces the influence of disease-induced index anomalies. This study highlighted the potential of integrating deep temporal modeling with ensemble regression for robust potato yield estimation, providing valuable support for precision agriculture and crop management under variable disease pressures.
Key words: UAV, multispectral, LSTM, XGBoost, potato, yield prediction.

Previsão da produtividade de batatas ao longo da safra a partir de imagens multiespectrais de veículo aéreo não tripulado usando um modelo híbrido LSTM-XGBoost sob condições de estresse causado por doenças

RESUMO: A batata é uma cultura alimentar e comercial fundamental na China, exigindo estimativa precisa de produtividade para agricultura de precisão e manejo oportuno de doenças. Este estudo foi realizado em 54 terrenos (3,5 m × 8 m) na província de Yunnan, com imagens multiespectrais coletadas por drones em quatro estágios fenológicos (emergência de brotos, início da floração, plena floração e senescência). Um modelo híbrido combinando redes neurais de Memória de Curto e Longo Prazo (LSTM) com o algoritmo Extreme Gradient Boosting (XGBoost) foi desenvolvido para explorar a dinâmica temporal e a capacidade de regressão. Além disso, em avaliações de estágio único, o modelo apresentou o melhor desempenho na senescência (R^2 = 0,939, RMSE = 856,4 kg ha^{-1}, MAE = 712,9 kg ha^{-1}), indicando forte correlação entre os índices de vegetação e a produtividade. Ao integrar todos os estágios, o modelo de sequência longa para terrenos saudáveis atingiu R^2 = 0,799, RMSE = 1598,4 kg ha^{-1} e MAE = 1465,9 kg ha^{-1}. A inclusão de cinco terrenos severamente doentes reduziu ligeiramente o desempenho (R^2 = 0,738), mas a precisão permaneceu aceitável. Para refletir as condições reais de cultivo, três tratamentos de doenças foram aplicados: terrenos inoculados com patógenos, parcelas com supressão de patógenos com extrato de rabanete e grupos com doenças naturais. Em todos esses cenários, o modelo LSTM-XGBoost superou consistentemente os modelos de regressão convencionais. Os resultados demonstram que a abordagem híbrida captura efetivamente a dinâmica de crescimento temporal e reduz a influência de anomalias de índice induzidas por doenças. Este estudo destaca o potencial da integração da modelagem temporal profunda com a regressão de conjunto para uma estimativa robusta da produtividade da batata, fornecendo suporte valioso para a agricultura de precisão e o manejo de culturas sob pressões variáveis de doenças.
Palavras-chave: UAV, multiespectral, LSTM, XGBoost, batata, previsão de produtividade.

INTRODUCTION

The global landscape of food security is increasingly precarious, characterized by a significant rise in the number of individuals experiencing food insecurity and a notable imbalance between supply and demand (VARZAKAS & SMAOUI, 2024). The potato, recognized as one of the most vital food crops

Received 08.25.25 Approved 11.11.25 Returned by the author 03.14.26
CR-2025-0457.R1
Editors: Leandro Souza da Silva Alberto Cargnelutti Filho

worldwide, is the largest non-cereal staple and plays a crucial role as an economic staple crop (PROGRESS OF POTATO STAPLE FOOD RESEARCH AND INDUSTRY DEVELOPMENT IN CHINA, 2017). Early forecasting of potato yields is essential not only for optimizing agricultural management but also for providing critical insights for the precise application of agrochemicals, pest and disease management, and efficient resource allocation. This, in turn, enhances productivity, minimizes waste, and promotes sustainable agricultural practices.

Unmanned aerial vehicle (UAV)-based remote sensing provides a rapid, flexible, and high-resolution alternative to satellite observations for assessing canopy characteristics, biomass, disease stress, and yield forecasting (OGLIARI et al., 2023; ZHANG & ZHU, 2023). Recent studies have confirmed its potential in crops such as wheat, sugar beet, and maize (SHEN et al., 2022; WANG et al., 2025a; ZHOU et al., 2017).

The rapid evolution of machine learning methodologies has promoted their widespread application in precision agriculture (BOTERO-VALENCIA et al., 2025). By analyzing UAV multispectral data, these algorithms can extract essential features and evaluate crop growth (LIU et al., 2024). Crops undergo distinct phenological stages, and integrating spectral information across stages allows for capturing temporal dynamics and understanding how early growth conditions affect final yield. However, potato yield is not solely determined by any single growth stage, as disease stress also plays a significant role (MAITO et al., 2025). Striking a balance between single-stage efficiency and multi-stage temporal dependency requires algorithms designed for sequence learning. Long Short-Term Memory (LSTM) networks can capture long-range temporal dependencies, while Extreme Gradient Boosting (XGBoost) is effective for nonlinear regression, making their combination particularly suitable for yield estimation tasks (MATEO-SANCHIS et al., 2023; WANG et al., 2023).

The yield of potatoes is affected by both phenological development and disease pressure. Accurately identifying growth phases that are most sensitive yielding response is vital for improving the practical utility of forecasting models. In this context, the present study proposes a hybrid framework that combines LSTM with XGBoost for potato yield estimation. The specific objectives are: (1) to assess the potential of UAV-based multispectral time-series data for forecasting potato yield; (2) to identify the phenological stages that provide the greatest predictive value; and (3) to evaluate the robustness of the proposed LSTM–XGBoost model under varying levels of disease interference.

MATERIALS AND METHODS

To systematically evaluate potato yield under varying disease conditions, we designed a hybrid framework that integrates UAV-based multispectral data acquisition, vegetation index extraction, and model development. The overall methodological workflow, including experimental design, image processing, feature extraction, and hybrid LSTM–XGBoost modeling, is summarized in figure 1.

Study area and experimental design

The experiment was conducted in Jiache Township, Huize County, Qujing City, Yunnan Province, China (103.40°E, 26.00°N, ~2000 m a.s.l.). The area has a temperate monsoon plateau climate with an annual mean temperature of ~10 °C and annual precipitation of ~1480 mm (LI & CHEN, 2015).

The experiment used certified potato seed tubers of the cultivar Hezuo-88, which is a locally adapted, high-yielding variety widely cultivated in Yunnan Province (WEN et al., 2024). A randomized-block experiment was established with 54 potato plots arranged in a 9 × 6 matrix (Figure 2). Each plot measured 3.5 × 8 m with 1 m buffer zones, and 225 plants were planted per plot (25 × 9 configuration, 0.25 m spacing, ~9 plants m^{-2}). To mimic real farming conditions, three disease treatments were applied: (1) Pathogen-inoculated plots, where each small plot was independently inoculated with a single soilborne or foliar pathogen, including *Alternaria solani* Sorauer, *Phytophthora infestans* (Mont.) de Bary, *Spongospora subterranea* (Wallr.) Lagerh., *Streptomyces scabies* (Thaxter) Waksman & Henrici, and *Meloidogyne* spp. The inoculum density for fungal and bacterial pathogens was adjusted to approximately 6.5×10^{12} CFU ha^{-1} (equivalent to the upper 15 cm soil layer) (EISFELD et al., 2022) and 10,000 potato cyst nematode eggs m^{-2} to simulate natural co-infestation (VAN HIMBEECK et al., 2025), applied by soil treatment before planting. (2) pathogen-suppressed plots, where the soil was treated with horseradish extract derived from the cruciferous plant Armoracia rusticana. Before planting, the extract was applied through drip irrigation under plastic mulch at a dosage of 200 kg ha^{-1}, followed by soil sealing and fumigation for 5 days; (3) natural-condition plots, where the soil was neither inoculated with pathogens nor treated with horseradish extract. These plots maintained the native soil microbial community, and diseases

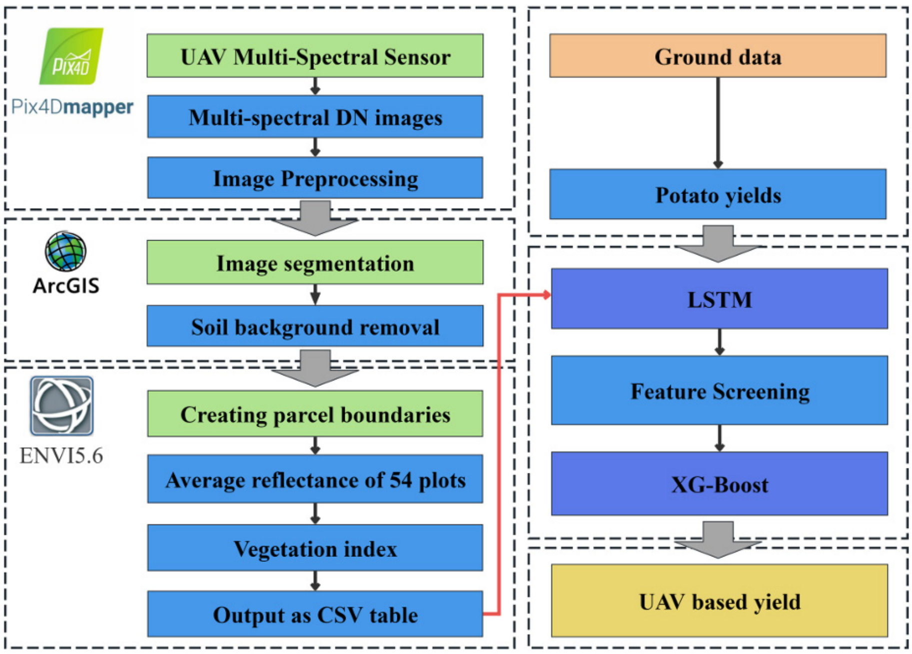

Figure 1 - Technical workflow for UAV-based potato yield estimation, including multispectral image acquisition and preprocessing (Pix4Dmapper), image segmentation and soil background removal, plot boundary delineation and reflectance/vegetation-index extraction (ArcGIS and ENVI), and yield modeling using long short-term memory (LSTM) and extreme gradient boosting (XGBoost). Outputs are exported as a comma-separated values (CSV) table. Abbreviations: UAV, unmanned aerial vehicle; DN, digital number; LSTM, long short-term memory; XGBoost, extreme gradient boosting.

developed naturally under local field conditions. The dominant naturally occurring pathogens in the area included Alternaria solani, Phytophthora infestans, and Streptomyces scabies (WENG et al., 2024). Four phenological stages were monitored: bud emergence (Q1), early flowering (Q2), full bloom (Q3), and senescence (Q4).

Data acquisition

Multispectral imagery was acquired using a DJI Phantom 4 Multispectral UAV equipped with an RGB camera and five multispectral sensors (Blue 450 ± 16 nm, Green 560 ± 16 nm, Red 650 ± 16 nm, Red Edge 730 ± 16 nm, Near-Infrared 840 ± 26 nm). Each sensor had a resolution of 1600 × 1300 pixels and a ground sampling distance of about 5 cm at 40 m altitude (Figure 3B). Each flight followed a pre-defined plan under clear conditions. Georeferencing was corrected by RTK-based ground control points (GCPs) (Figure 3C), and radiometric calibration was performed using a reflectance panel (Figure 3D). Orthomosaics were processed in Pix4Dmapper and cropped in ENVI to match plot boundaries. Non-vegetation pixels were masked, and mean reflectance values were extracted for further analysis.

Selection of spectral indices

A total of 39 vegetation indices (VIs) were computed from the five spectral bands to characterize canopy condition and stress response (Table 1). Representative examples include NDVI (Normalized Difference Vegetation Index) (ROUSE et al., 1974), EVI (Enhanced Vegetation Index) (HUETE et al., 2002), and NDRE (Normalized Difference Red-Edge Index)(GITELSON & MERZLYAK, 1994).

Regression techniques

A hybrid framework was designed combining Long Short-Term Memory (LSTM) networks and Extreme Gradient Boosting (XGBoost). The architecture of the LSTM cell, which enables the modeling of long-range temporal dependencies through memory units and gating mechanisms, is illustrated in figure 4. Stacked LSTM layers were

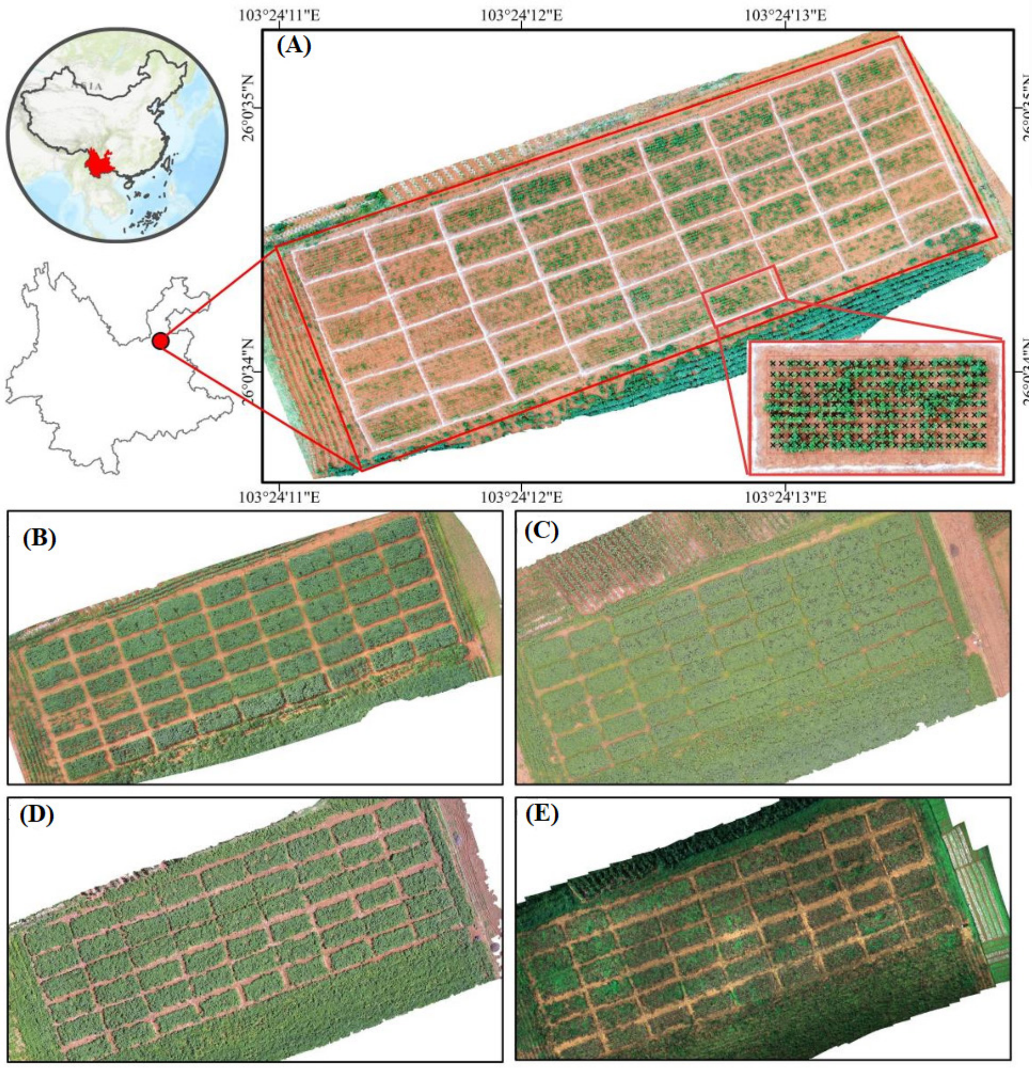

Figure 2 - (A) Location of the study area and layout of the 54 experimental potato plots; the inset at the bottom right shows the planting density scheme; (B) RGB (red–green–blue) image of the potato canopy at the bud-emergence stage; (C) RGB image at the early-flowering stage; (D) RGB image at the full-bloom stage; (E) RGB image at the senescence stage.

employed to extract temporal features from vegetation index sequences across phenological stages (WANG et al., 2023). These high-level temporal embeddings were then passed into an XGBoost regressor, which modeled the nonlinear relationships between spectral features and yield (CHEN & GUESTRIN, 2017; MATEO-SANCHIS et al., 2023). The overall hybrid workflow, integrating sequential feature extraction by LSTM with regression by XGBoost, is depicted in figure 5, highlighting its application across four phenological stages: bud emergence (Q1), initial flowering (Q2), full flowering (Q3), and senescence (Q4). This integration leveraged the sequential learning capacity of LSTM and the strong regression capability of XGBoost, enabling robust predictions under heterogeneous and disease-affected conditions.

Model testing and evaluation metrics

The dataset was divided into training (80%) and testing (20%) subsets. Model performance was assessed using the coefficient of determination (R^2), root mean squared error (RMSE), and mean absolute

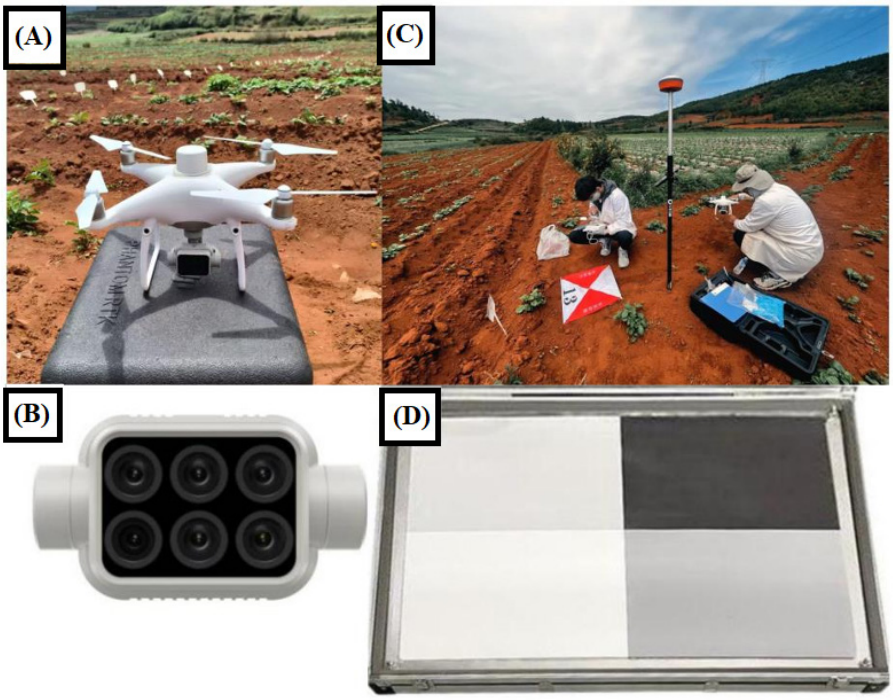

Figure 3 - Equipment used in this study:(A) DJI (Da-Jiang Innovations) Phantom 4 Multispectral unmanned aerial vehicle (UAV) equipped with an integrated multispectral imaging system; (B) Multispectral sensor, comprising one true-color camera and five multispectral cameras (blue, green, red, red-edge, and near-infrared) for visible and multispectral imaging;(C) real-time kinematic （RTK） unit for establishing ground control points for UAV imagery; (D) Calibration panel for reflectance calibration of the multispectral sensor.

error (MAE). Smaller RMSE and MAE values indicate better predictive accuracy. These metrics were calculated following standard definitions. The expressions are as follows:

$$R^2 = 1 - \frac{\sum_{i-1}^{n} (\hat{y}_i - y_i)^2}{\sum_{i-1}^{n} (y_i - \bar{y})^2} \quad (1)$$

$$RMSE = \sqrt{\frac{1}{n} \sum_{i-1}^{n} (y_i - \hat{y}_i)^2} \quad (2)$$

$$MAE = \frac{1}{n} \sum_{i=n}^{n} |y_i - \hat{y}_i| \quad (3)$$

n represents the total number of samples in the test set. yi and ŷi represent the measured and predicted values of biomass, respectively. ȳ represents the average of the measured biomass values.

RESULTS AND DISCUSSION

Potato yields exhibited significant variation across the three disease-management treatments (Figure 6). The pathogen-inoculated treatment recorded the lowest mean yield of 24,594.44 ± 12.20 kg ha^{-1}, reflecting the considerable suppression caused by artificial pathogen pressure. The natural-condition group yielded an intermediate mean of 28,776.79 ± 12.81 kg ha^{-1}, suggesting the presence of ambient disease effects. Conversely, the pathogen-suppressed treatment achieved the highest average yield of 30,298.61 ± 7.47 kg ha^{-1}, indicating that horseradish-extract soil treatment effectively alleviated disease stress and improved plant health (LI et al., 2023; REN et al., 2018). These quantitative results demonstrated the strong influence of disease management on productivity and provide a useful foundation for evaluating the robustness of subsequent yield-prediction models.

The spectral reflectance dynamics across the four phenological stages further supported these yield patterns (Figure 7). From early flowering (Q2) to full bloom (Q3), canopy reflectance increased in all spectral bands, particularly in the red-edge and near-infrared regions. A slight decline occurred

Table 1 - Overview of Vegetation Indices.

Vegetation Index	Equation
NDVI（Normalized difference vegetation index）	$NDVI = \frac{NIR - R}{NIR + R}$
RTVI（Red-edge triangular vegetation index）	RTVI=100×(NIR-RE)-10×(NIR-G)
RVI（Ratio vegetation index）	RVI=NIR/R
TCARI（Transformed chlorophyll absorption in reflectance index）	TCARI=3.0×[(RE-R)-0.2×(RE-G)×(RE/R)]
WDRI（Wide dynamic range index）	$WDRI = \frac{0.3\times NIR - R}{0.3\times NIR + R}$
GRVI（Green-red vegetation index）	$GDVI = \frac{G - R}{G + R}$
Ari（Anthocyanin reflectance index）	Ari = NIR×[(1.0/G)−(1.0/RE)]
Cri（Carotenoid reflectance index）	Cri=（1.0/G）－（1.0/RE）
Datt（Datt’s chlorophyll content）	$Datt = \frac{NIR - RE}{NIR - R}$
Dvi（Difference vegetation index）	Dvi = NIR − R
ENDVI（Enhanced normalized difference vegetation index）	$ENDVI = \frac{NIR + 2.0\times B}{NIR + G + 2.0\times B}$
EVI（Enhanced vegetation index）	$EVI = 2.5\times\frac{NIR - R}{6\times R - 7.5\times B + 1}$
EVI2（Enhanced vegetation index without a blue band）	$EVI2 = 2.5\times\frac{NIR - R}{NIR + 2.4R + 1}$
Gci（Green chlorophyll index）	Gci=(NIR/G)−1.0
GNDVI（Green normalized difference vegetation index）	$GNDVI = 2.5\times\frac{NIR - G}{NIR + G}$
Mtci（MERIS terrestrial chlorophyll index）	$Mtci = \frac{NIR - RE}{RE - R}$
MCARI（Modified chlorophyll absorption ratio index）	MCARI=（RE/R）×[（RE-R）-0.2×（RE-G）]
MCARI2（Modified chlorophyll absorption ratio index 2）	MCARI_2 = 1.2×(2.5 × (NIR−R)−1.3 × (NIR−G))
MCARI3（Modified chlorophyll absorption ratio index 3）	MCARI_3= 1.5 × (2.5 × (NIR−R) −1.3 × (NIR−G))
Msavi（Modified soil-adjusted vegetation index）	$MSAVI = \frac{2\times NIR + 1 - \sqrt{(2\times NIR + 1)^2 - 8\times(NIR - R)}}{2}$
MTVI2（Modified triangular vegetation index）	$MTVI2 = \frac{1.5\times[1.2\times(NIR - G) - 2.5\times(R - G)}{\sqrt{(2\times NIR + 1)^2 - (6\times NIR - 5\sqrt{R}) - 0.5}}$
NDCI（Normalized difference cloud index）	$NDCI = 2.5\times\frac{RE - G}{RE + G}$
Ndre（Normalized difference red edge index）	$NDRE = \frac{NIR - RE}{NIR + RE}$
Nexg（Normalized excess green index）	$Nexg = \frac{2\times G - R + B}{G + R + B}$
Npci（normalized total pigment to chlorophyll a ratio index）	$Npci = \frac{R - B}{R + B}$
OSAVI（Optimized soil-adjusted vegetation index）	$OSAVI = \frac{NIR + R}{NIR + R + 0.16}$
Rvi（Ratio vegetation index）	$RVI = \frac{NIR}{R}$
Reci（Red edge chlorophyll index）	$RECI = \frac{NIR}{RE} - 1$
Reri（Red edge relative index）	$RERI = \frac{RE - R}{NIR}$
Rgvi（Red-green ratio vegetation index）	$RVI = \frac{R}{G}$
RDVI（Renormalized Difference Vegetation Index)）	$RDVI = \frac{NIR - R}{\sqrt{(NIR + R)}}$
SRPI（Simple ratio pigment index）	$SRPI = \frac{B}{R}$
TVI（Triangular vegetation index）	Tvi =60.0 × (NIR − G) −100.0 × (R − G)
EXR（Excess red index）	EXR=1.4 × R-G
EXG（Excess green index）	EXR=2 × G - R - B
EXB（Excess blue index）	EXB=1.4 × B-G
EXGR（Excess Green Index）	ExGE=(2G - R - B) - (1.4R - G)
VDVI（Vegetation Drought Index）	$VDVI = \frac{2G - R - B}{2G + R + B}$
MSR（Modified Soil Adjusted Vegetation Index）	$MSR = \frac{NIR}{R} - 1$

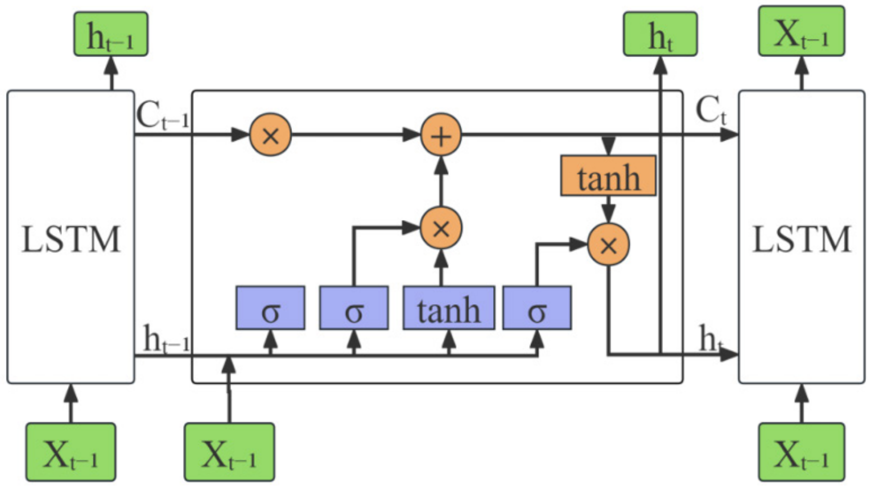

Figure 4 - Long short-term memory （LSTM） cell. The diagram illustrates the flow of information through the cell state (C_t) and hidden state (h_t), including the forget, input, and output gates. Here, X_t denotes the input at time *t*, σ represents the sigmoid activation function, and tanh represents the hyperbolic tangent activation function.

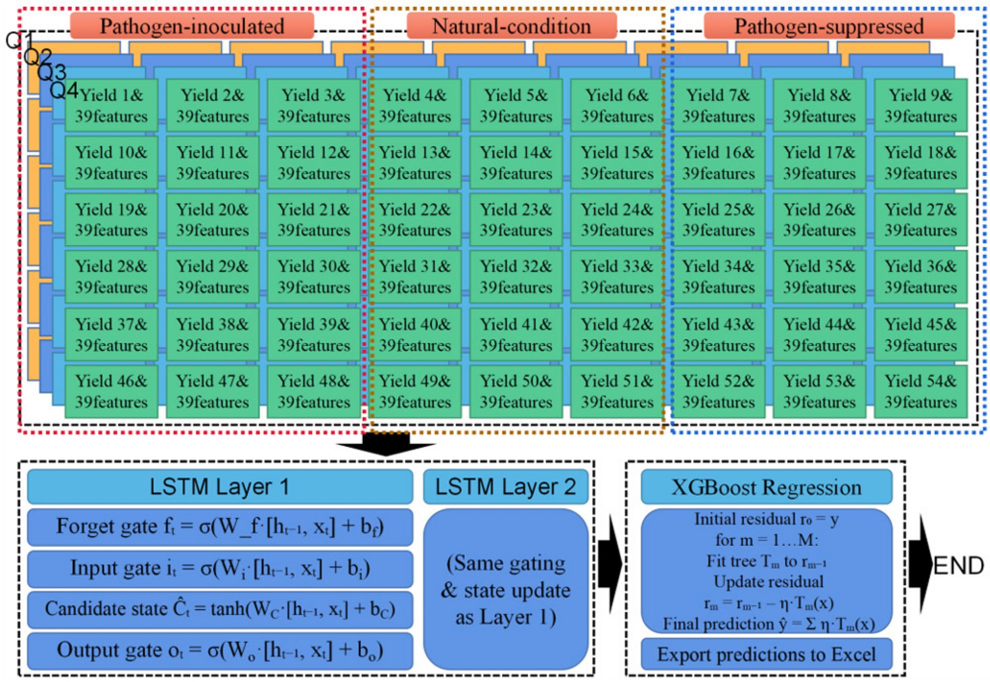

Figure 5 - XGBoost-LSTM schematic. Bud stage (Q1), Initial flowering stage (Q2), Full flowering stage (Q3), and End of flowering stage (Q4).

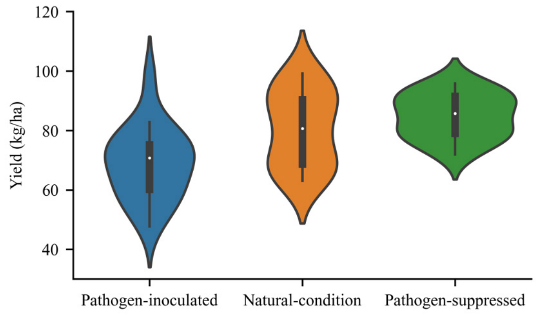

Figure 6 - Violin plots showing the distribution of potato yields under three disease-management treatments.

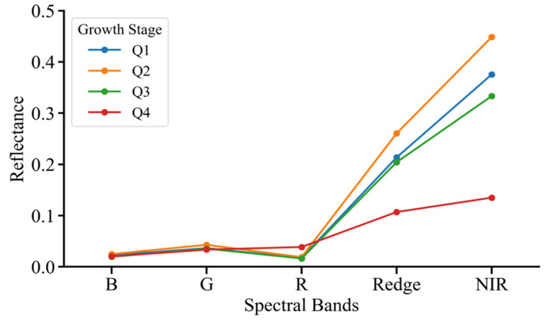

Figure 7 - Temporal trends of mean potato-canopy reflectance across different spectral bands at four phenological stages. Q1, Q2, Q3, and Q4 correspond to the bud stage, initial flowering stage, full flowering stage, and end of flowering stage, respectively.

between Q2 and Q3, reflecting the transition to reproductive growth and leaf senescence. By the senescence stage (Q4), a marked increase in red-band reflectance and a sharp decline in red-edge and near-infrared reflectance were observed, consistent with chlorophyll degradation and canopy thinning. This spectral behavior highlighted the sensitivity of red-edge and NIR wavelengths to potato physiological status, aligning with previous findings (ANDEREGG et al., 2020; LIU et al., 2020).

Correlation analysis confirmed that vegetation indices derived at Q4 were most strongly associated with final yield (Figure 8). Twenty-four indices exceeded the threshold correlation, compared to only 12–19 in earlier stages. This suggested that senescence provides the most reliable spectral signals for

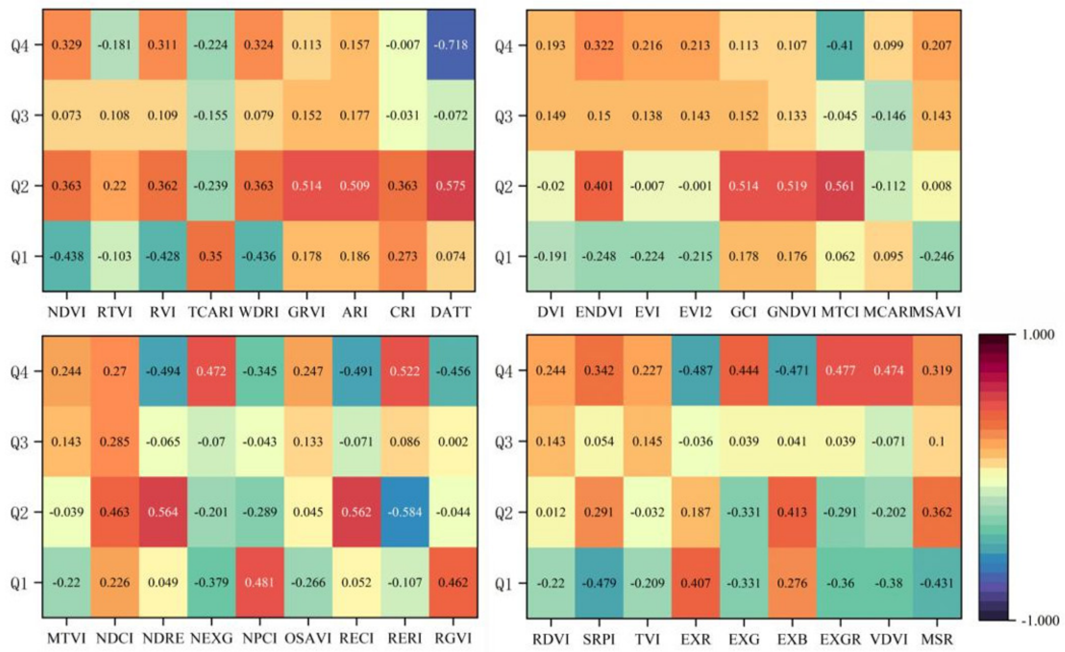

Figure 8 - Correlation between vegetation indices and yield.

estimating harvestable biomass, as tuber accumulation stabilizes and canopy spectral features directly reflect final yield potential. Such stage-dependent differences explain why late-season imagery is consistently more predictive of yield, corroborating earlier reports in potato and other crops (GÓMEZ et al., 2019).

Model performance reflected these physiological and spectral dynamics. Across datasets with varying disease inclusion, the LSTM–XGBoost consistently outperformed XGBoost alone (Table 2; Table 3). For single-stage modeling, the senescence stage achieved the highest predictive accuracy, with R^2 = 0.939, RMSE = 865.4 kg ha^{-1}, and MAE = 712.9 kg ha^{-1} in healthy plots. In contrast, performance declined at earlier stages, particularly at full bloom (Q3), where canopy variability and stress interactions weakened correlations with yield. The superior accuracy of Q4 models reflects the strong alignment between senescence spectral traits and final tuber biomass, which is consistent with findings by (GOMEZ et al., 2024), who also reported that potato yield prediction accuracy improves as the crop approaches harvest.

When temporal features from all four stages were fused, prediction accuracy improved compared with Q1–Q3 alone but remained slightly lower than the Q4 single-stage model (Table 3; Figure 9, Figure 10, Figure 11). This apparent paradox arises because early-stage indices capture growth processes that only indirectly relate to yield, while senescence indices reflect the final biomass accumulation. Thus, concatenating multiple stages introduces additional variability without proportionate predictive gain. Similar observations were noted in wheat and maize

Table 2 - Potato yield estimation results based on features extracted from individual phenological stages.

Algorithm	Treatment	Phenological Stage	---------------------Training--------------------			--------------------Validation--------------------		
			R2	RMSE (kg/ha)	MAE (kg/ha)	R2	RMSE (kg/ha)	MAE (kg/ha)
XGBoost	LIPS	Q1	0.732	1848.572	1421.268	0.756	2114.896	1885.331
		Q2	0.452	2822.120	2268.951	0.442	2619.303	2344.935
		Q3	0.182	3469.025	2836.255	0.184	2870.305	2683.523
		Q4	0.549	2501.631	1987.132	0.551	2218.408	1614.345
LSTM + XGBoost	LIPS	Q1	0.886	1341.481	1051.326	0.724	1480.237	1210.034
		Q2	0.959	745.378	574.383	0.789	1795.196	1357.599
		Q3	0.849	1535.595	1334.986	0.626	1785.583	1612.745
		Q4	0.929	979.322	822.568	0.939	865.384	712.917
XGBoost	MIPS	Q1	0.281	4122.844	2548.999	0.345	3821.553	3399.496
		Q2	0.490	3461.693	2264.022	0.586	3148.319	2444.806
		Q3	0.163	4440.557	3605.921	0.150	4524.331	3989.874
		Q4	0.733	2348.569	1578.440	0.717	2998.469	2564.911
LSTM + XGBoost	MIPS	Q1	0.718	2619.783	2107.653	0.729	2271.363	1936.155
		Q2	0.798	2344.240	1876.346	0.624	2009.590	1370.584
		Q3	0.539	3574.585	3051.828	0.488	2124.401	1873.165
		Q4	0.911	1503.120	1221849	0.908	1228.361	1035.636
XGBoost	APS	Q1	0.395	3503.881	2663.945	0.421	3550.558	2998.718
		Q2	0.518	3227.269	2630.597	0.530	2795.116	2060.017
		Q3	0.514	3238.610	2534.801	0.510	2833.337	2586.811
		Q4	0.533	3263.784	2719.440	0.522	2302.973	1912.839
LSTM + XGBoost	APS	Q1	0.736	2353.533	1955.509	0.612	2624.601	2160.443
		Q2	0.699	2552.296	2017.878	0.582	2635.194	2290.157
		Q3	0.760	2235.213	1651.030	0.563	2695.474	2358.450
		Q4	0.816	1967.486	1528.537	0.855	1605.567	1145.229

Table 3 - Potato yield estimation results based on features extracted from all four phenological stages.

Algorithm	Treatment	-----Training-----			-----Validation-----		
		R2	RMSE (kg/ha)	MAE (kg/ha)	R2	RMSE (kg/ha)	MAE (kg/ha)
LSTM	LIPS	0.675	2000.983	1602.128	0.746	1918.291	1592.451
LSTM + XGBoost		0.840	1469.071	1192.334	0.790	1598.411	1465.921
LSTM	MIPS	0.623	2989.005	2378.417	0.610	2965.998	2294.877
LSTM + XGBoost		0.792	2332.053	1905.326	0.738	1783.842	1336.048
LSTM	APS	0.544	2935.003	2336.969	0.573	2722.240	2428.533
LSTM + XGBoost		0.736	2353.533	1955.509	0.612	2624.601	2160.443

yield studies, where late-season data often surpassed multi-stage models (SHEN et al., 2022; WANG et al., 2025a). Nonetheless, the multistage fusion framework still demonstrated strong capacity for generalization, particularly when disease-affected plots were included, highlighting its robustness in heterogeneous field conditions.

Comparisons with conventional regressors (XGBoost, SVR, PLSR, RF) further underscored the superiority of the LSTM–XGBoost hybrid (Figure 12). While traditional methods exhibited unstable fits and even distorted relationships under disease stress, the hybrid consistently delivered higher R^2 values and lower errors across stages and datasets. This advantage can be attributed to the LSTM's ability to capture temporal dependencies and denoise vegetation index sequences, thereby enhancing the subsequent XGBoost regression. The synergy

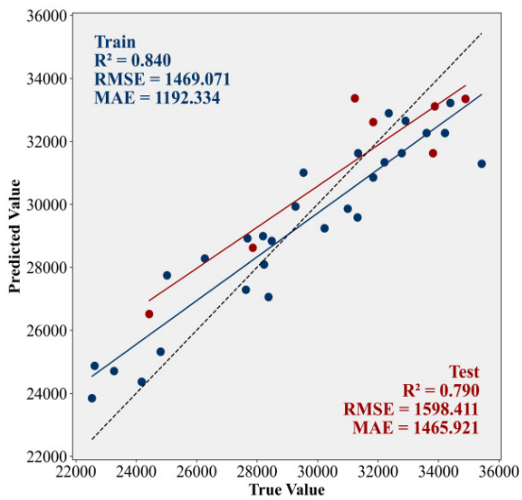

Figure 9 - Comparison of long-sequence yield-prediction performance on healthy plots. Note: The x-axis denotes predicted yield (kg ha^{-1}) and the y-axis denotes observed yield (kg ha^{-1}). The black dashed line represents the 1:1 ideal fit, the blue solid line is the training-set regression, and the red solid line is the test-set regression.

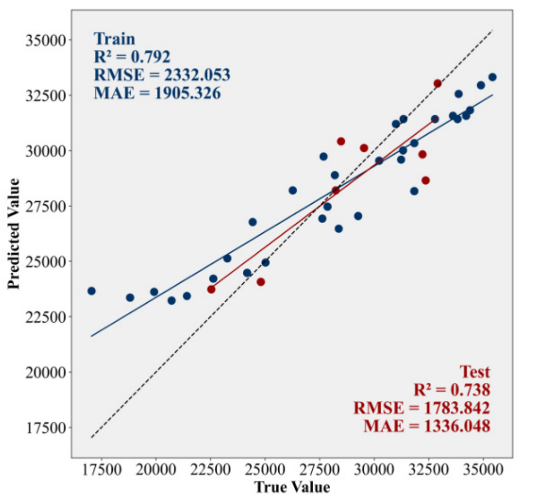

Figure 10 - Comparison of long-sequence yield-prediction performance after incorporating diseased plots into the healthy-plot dataset. Note: The x-axis represents predicted yield (kg ha^{-1}) and the y-axis represents observed yield (kg ha^{-1}). The black dashed line denotes the 1:1 ideal fit; the blue solid line indicates the training-set regression; and the red solid line indicates the test-set regression.

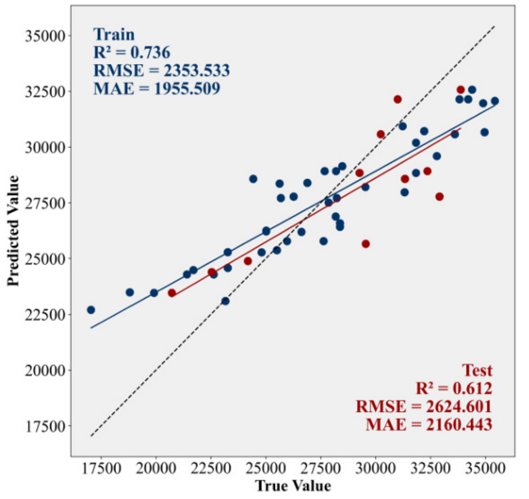

Figure 11 - Comparison of long-sequence yield-prediction performance across all plots. Note: The x-axis represents predicted yield (kg ha-1) and the y-axis represents observed yield (kg ha-1). The black dashed line denotes the 1:1 ideal fit; the blue solid line indicates the training-set regression; and the red solid line indicates the test-set regression.

between temporal feature learning and nonlinear regression explains the superior performance observed here and aligns with earlier demonstrations of deep learning's benefits in precision agriculture (MATEO-SANCHIS et al., 2023).

The impact of pathogen stress on spectral–yield relationships was evident in all modeling scenarios. Incorporating diseased plots consistently reduced accuracy compared with healthy-only datasets (Figures 13, Figure 14, Figure 15). Pathogen infection alters chloroplast function, reduces chlorophyll content, and disrupts water transport, leading to abrupt changes in red and NIR reflectance (LI et al., 2021). These spectral anomalies weaken vegetation index–yield correlations, thereby lowering prediction accuracy. The most substantial reductions occurred at early stages, when disease interference distorted canopy development signals. By senescence; however, the strong physiological link to tuber biomass helped stabilize predictive performance, even in diseased plots. This finding emphasized the importance of stage selection in practical yield-forecasting applications under real-world stress conditions.

Taken together, the results demonstrated that UAV-based multispectral imagery provides a powerful basis for potato yield estimation, particularly when integrated with hybrid temporal–regression models. The LSTM–XGBoost framework achieved robust performance across varying disease scenarios, confirming its applicability to precision agriculture under heterogeneous field conditions. Although, all UAV flights were conducted under clear-sky conditions and radiometric calibration was applied to minimize illumination differences, short-term variations in solar radiation intensity, humidity, and wind speed may still have slightly influenced canopy reflectance and spectral consistency (MAES, 2025). These microclimatic fluctuations could partially explain minor variations in vegetation

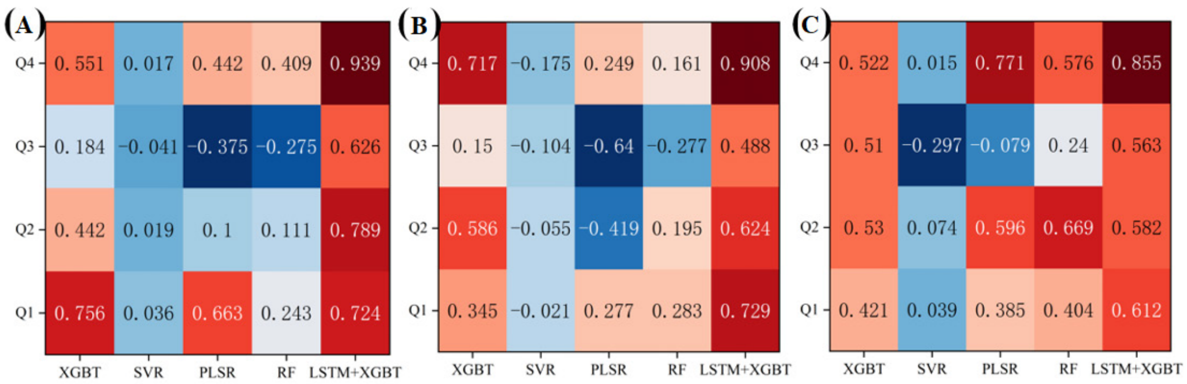

Figure 12 - Comparison of predictive performance between the LSTM–XGBoost hybrid and conventional models across plot groups:(A) Lightly Infected Plot Subse;(B) Mixed-Infection Plot Subset;(C) All-Plot Sample Set.

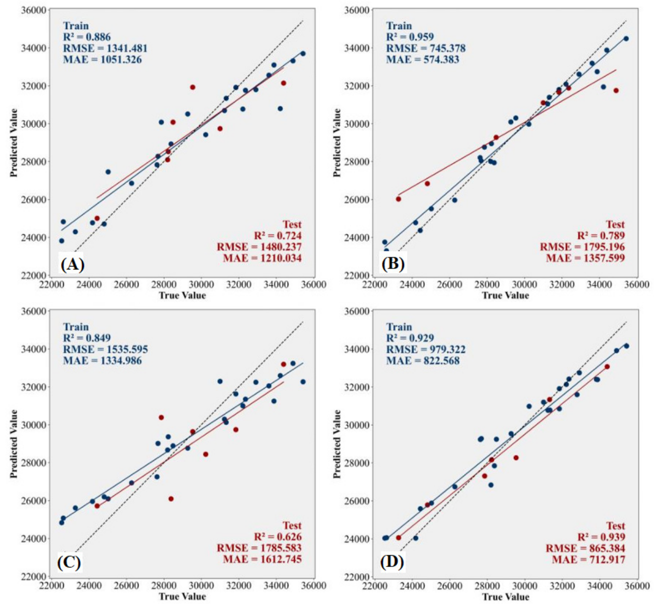

Figure 13 - Comparison of single-stage yield-prediction performance on healthy plots: (A) bud emergence; (B) early flowering; (C) full bloom; (D) senescence. Note: The x-axis denotes predicted yield (kg ha^{-1}) and the y-axis denotes observed yield (kg ha^{-1}). The black dashed line represents the 1:1 ideal fit; the blue solid line depicts the training-set regression; and the red solid line depicts the test-set regression.

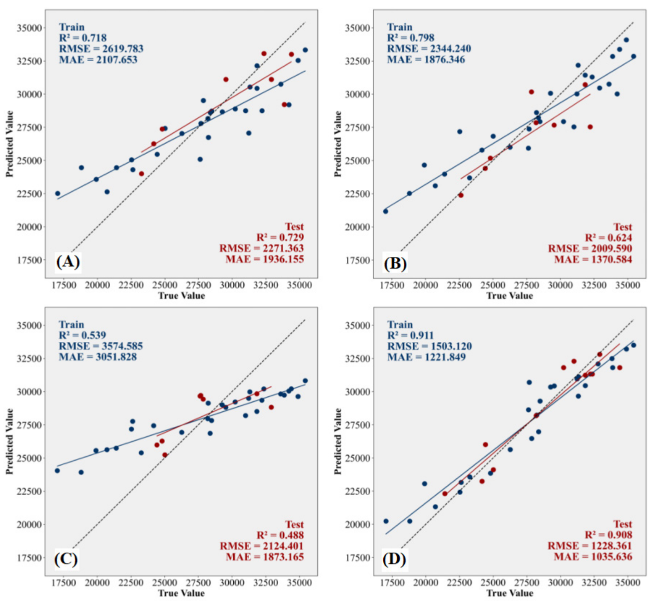

Figure 14 - Comparison of single-stage yield-prediction performance after incorporating diseased plots into the healthy-plot dataset: (A) bud emergence; (B) early flowering; (C) full bloom; (D) senescence. Note: The x-axis denotes predicted yield (kg ha^{-1}), and the y-axis denotes observed yield (kg ha^{-1}). The black dashed line represents the 1:1 ideal fit; the blue solid line represents the training-set regression; and the red solid line represents the test-set regression.

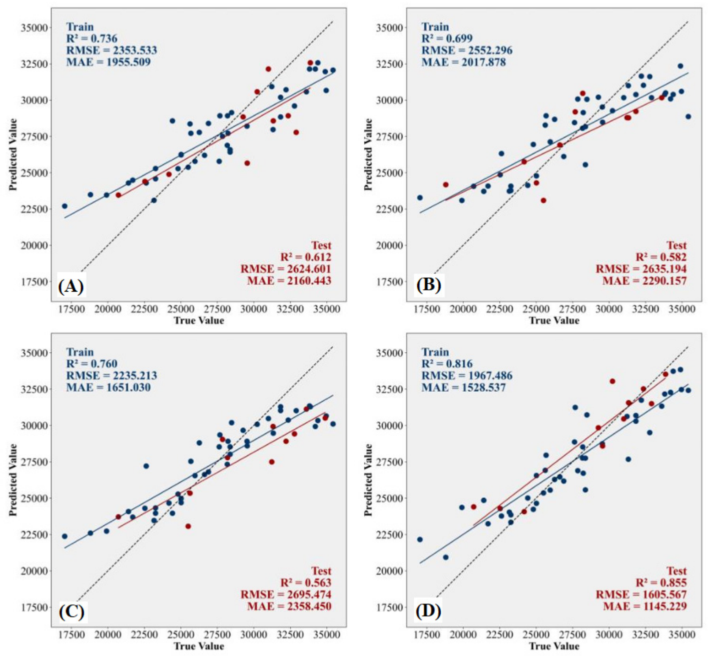

Figure 15 - Comparison of single-stage yield-prediction performance across all plots: (A) bud emergence; (B) early flowering; (C) full bloom; (D) senescence. Note: The x-axis denotes predicted yield (kg ha^{-1}), and the y-axis denotes observed yield (kg ha^{-1}). The black dashed line represents the 1:1 ideal fit; the blue solid line represents the training-set regression; and the red solid line represents the test-set regression.

indices among flight dates. Future studies should incorporate concurrent meteorological data to further enhance model robustness under variable field conditions (WANG et al., 2025b). Moreover, the analysis underscores the physiological rationale for the superior predictive power of senescence imagery, highlights the limitations of early-stage modeling, and affirmed the necessity of integrating disease factors into yield-forecasting frameworks. These insights not only validated the effectiveness of the proposed methodology but also provided guidance for future efforts to improve yield prediction through advanced modeling of crop growth dynamics under stress.

CONCLUSION

This study developed a hybrid LSTM–XGBoost framework for potato yield estimation using UAV-based multispectral time-series data across four phenological stages. The model effectively captured temporal growth dynamics, with the senescence stage providing the highest predictive accuracy ($R^2 \approx 0.94$). Importantly, the framework demonstrated robustness under varying levels of disease stress, maintaining reliable performance even when severely diseased plots were included.

These findings confirmed the applicability of the proposed approach for precision yield forecasting and disease monitoring in potato production. Future work should extend the framework to multiple cultivars and agro-ecological regions, thereby enhancing its generalizability and supporting wider adoption in precision agriculture.

ACKNOWLEDGMENTS

The authors sincerely acknowledge the Key Laboratory of Plant Pathology, College of Plant Protection, Yunnan Agricultural University, for providing experimental support in the implementation of disease treatments.This research was funded by the sub-project of the National Key Research and Development Program of China, “Demonstration and Application of Drought-Resistant, Water-Conserving, and Productivity-Enhancing Technologies for Sloping Farmland in Southeastern Yunnan” (Grant No. 2022YFD1901504-05).

DECLARATION OF CONFLICT OF INTEREST

The authors declare no conflict of interest. The founding sponsors had no role in the design of the study; in the collection, analyses, or interpretation of data; in the writing of the manuscript, and in the decision to publish the results.

AUTHORS' CONTRIBUTIONS

ST and YP contributed equally to this work. ST and YP were responsible for conceptualization, methodology, data analysis, and manuscript drafting. JD and JX contributed to data curation and preliminary analysis. JG, JL, and YZ participated in data processing and validation. FW provided technical support and assisted with result interpretation. JL supervised the study, contributed to funding acquisition, and revised the manuscript. All authors reviewed and approved the final version of the manuscript.

DATA AVAILABILITY STATEMENT

Data sharing is not applicable to this article, as no publicly available datasets were generated or analyzed during the current study.

DECLARATION OF USE OF ARTIFICIAL INTELLIGENCE

The authors declare that no artificial intelligence tools were used in the design, analysis, or writing of this manuscript.

REFERENCES

ANDEREGG, J. et al. Spectral vegetation indices to track Senescence Dynamics in Diverse Wheat Germplasm. **Frontiers in Plant Science**, v.10, 2020. Available from: <https://www.frontiersin.org/article/10.3389/fpls.2019.01749/full>. Accessed: Aug. 27, 2025.

BOTERO-VALENCIA, J. et al. Machine learning in sustainable agriculture: Systematic Review and Research Perspectives. **Agriculture**, v.15, n.4, p.377, 2025. Available from: <https://www.mdpi.com/2077-0472/15/4/377>. Accessed: Aug. 26, 2025.

CHEN, T.; GUESTRIN, C. Xgboost: Reliable large-scale tree boosting system. In: Proceedings of the 22nd Sigkdd Conference on Knowledge Discovery and Data Mining, 2017, **Anais** [...], p.13-17, 2017. Available from: <http://learningsys.org/papers/LearningSys_2015_paper_32.pdf>. Accessed: May, 07, 2025.

EISFELD, C. et al. Dose-response relationship of Ralstonia solanacearum and potato in greenhouse and in vitro experiments. **Frontiers in Plant Science**, v.13, p.1074192, 2022. Available from: <https://www.frontiersin.org/articles/10.3389/fpls.2022.1074192/full>. Accessed: Oct. 13, 2025.

GITELSON, A.; MERZLYAK, M. N. Quantitative estimation of chlorophyll-a using reflectance spectra: Experiments with autumn chestnut and maple leaves. **Journal of Photochemistry and Photobiology B: Biology**, v.22, n.3, p.247-252, 1994. Available from: <https://linkinghub.elsevier.com/retrieve/pii/1011134493069634>. Accessed: May, 07, 2025.

GOMEZ, D. et al. Detecting sensitive spectral bands and vegetation indices for potato yield using handheld spectroradiometer data. **Plants**, v.13, n.23, p.3436, 2024. Available from: <https://www.mdpi.com/2223-7747/13/23/3436>. Accessed: Aug. 27, 2025.

GÓMEZ, D. et al. Potato yield prediction using machine learning techniques and sentinel 2 data. **Remote Sensing**, v.11, n.15, p.1745, 2019. Available from: <https://www.mdpi.com/2072-4292/11/15/1745>. Accessed: Jun. 01, 2025.

HUETE, A. et al. Overview of the radiometric and biophysical performance of the MODIS vegetation indices. **Remote Sensing of Environment**, v.83, n.1-2, The Moderate Resolution Imaging Spectroradiometer (MODIS): a new generation of Land Surface Monitoring, p.195–213, 2002. Available from: <https://linkinghub.elsevier.com/retrieve/pii/S0034425702000962>. Accessed: May, 07, 2025.

LI, L.; CHEN, X. **The administrative divisions of the People's Republic of China**: Yunnan province volume. Beijing: China Social Sciences Press, 2015. 2015. (The administrative divisions of the People's Republic of China).

LI, Y. et al. Effects of allyl isothiocyanate fumigation on medicinal plant root knot disease control, plant survival, and the soil bacterial community. **BMC Microbiology**, v.23, n.1, p 278, 2023. Available from: <https://bmcmicrobiol.biomedcentral.com/articles/10.1186/s12866-023-02992-w>. Accessed: Aug. 27, 2025.

LI, D. et al. Improving potato yield prediction by combining cultivar information and UAV remote sensing data using machine learning. **Remote Sensing**, v.13, n.16, p.3322, 2021. Available from: <https://www.mdpi.com/2072-4292/13/16/3322>. Accessed: May, 30, 2025.

LIU, T. et al. The estimation of wheat yield combined with UAV canopy spectral and volumetric data. **Food and Energy Security**, v.13, n.1, 2024. Available from: <https://onlinelibrary.wiley.com/doi/10.1002/fes3.527>. Accessed: Aug. 26, 2025.

LIU, N. et al. Growth stages classification of potato crop based on analysis of spectral response and variables optimization. **Sensors**, v.20, n.14, p.3995, 2020. Available from: <https://www.mdpi.com/1424-8220/20/14/3995>. Accessed: Aug. 27, 2025.

MAES, W. H. Practical guidelines for performing UAV mapping flights with snapshot sensors. **Remote Sensing**, v.17, n.4, p.606, 2025. Available from: <https://www.mdpi.com/2072-4292/17/4/606>. Accessed: Oct. 13, 2025.

MAITO, G. et al. Potato late blight control based on the Blitecast forecast system on the Rio Grande do Sul Plateau, Brazil. **Ciência Rural**, v.55, n.4, p.e20230691, 2025. Available from: <http://www.scielo.br/scielo.php?script=sci_arttext&pid=S0103-84782025000400151&tlng=en>. Accessed: Aug. 26, 2025.

MATEO-SANCHIS, A. et al. Interpretable long short-term memory networks for crop yield estimation. **IEEE Geoscience and Remote Sensing Letters**, v.20, p.1-5, 2023. Available from: <https://ieeexplore.ieee.org/document/10041987/>. Accessed: May, 07, 2025.

OGLIARI, D. G. P. et al. Airborne cameras for natural grassland classification in the Pampa biome. **Ciência Rural**, v.53, n.2, p.e20210765, 2023. Available from: <http://www.scielo.br/scielo.php?script=sci_arttext&pid=S0103-84782023000200201&tlng=en>. Accessed: Aug. 26, 2025.

ZHANG, H. et al. Progress of potato staple food research and industry development in China. **Journal of Integrative Agriculture**, v.16, n.12, p.2924-2932, 2017. Available from: <https://linkinghub.elsevier.com/retrieve/pii/S2095311917617362>. Accessed: Aug. 26, 2025.

REN, Z. et al. Evaluation of allyl isothiocyanate as a soil fumigant against soil-borne diseases in commercial tomato (*Lycopersicon esculentum* Mill.) production in China. **Pest Management Science**, v.74, n.9, p.2146-2155, 2018. Available from: <https://onlinelibrary.wiley.com/doi/10.1002/ps.4911>. Accessed: Aug. 27, 2025.

ROUSE, J. W. et al. **Monitoring the Vernal Advancement and Retrogradation (Green Wave Effect) of Natural Vegetation**. 1974. Available from: <https://ntrs.nasa.gov/citations/19750020419>. Accessed: Apr. 10, 2025.

SHEN, Y. et al. Improving Wheat Yield Prediction Accuracy Using LSTM-RF Framework Based on UAV Thermal Infrared and Multispectral Imagery. **Agriculture**, v.12, n.6, p.892, 2022. Available from: <https://www.mdpi.com/2077-0472/12/6/892>. Accessed: Mar. 06, 2025.

VAN HIMBEECK, R. et al. Patchy distribution of potato cyst nematodes within single arable fields reveals local disease suppressiveness mediated by disparate microbial communities. **Environmental Microbiology**, v.27, n.5, p.e70113, 2025. Available from: <https://sfamjournals.onlinelibrary.wiley.com/doi/10.1111/1462-2920.70113>. Accessed: Oct. 13, 2025.

VARZAKAS, T.; SMAOUI, S. Global food security and sustainability issues: The road to 2030 from nutrition and sustainable healthy diets to food systems change. **Foods**, v.13, n.2, p.306, 2024. Available from: https://www.mdpi.com/2304-8158/13/2/306. Accessed: Jun. 20, 2025.

WANG, Q. et al. Prediction of sugar beet yield and quality parameters using stacked-LSTM model with pre-harvest UAV time series data and meteorological factors. **Artificial Intelligence in Agriculture**, p.S2589721725000236, 2025a. Available from: <https://linkinghub.elsevier.com/retrieve/pii/S2589721725000236>. Accessed: Mar. 06, 2025.

WANG, T. et al. Drought prediction: Insights from the fusion of LSTM and multi-source factors. **Science of The Total Environment**, v.902, p.166361, 2023. Available from: <https://linkinghub.elsevier.com/retrieve/pii/S0048969723049860>. Accessed: May, 07, 2025.

WANG, M. et al. Unmanned aerial vehicle (UAV) imagery for plant communities: optimizing visible light vegetation index to extract multi-species coverage. **Plants**, v.14, n.11, p.1677, 2025b. Available from: https://www.mdpi.com/2223-7747/14/11/1677. Accessed: Oct. 13, 2025.

WEN, L. et al. Effect of photoperiod on dry matter accumulation and partitioning in potato. **Agriculture**, v.14, n.7, p.1156, 2024. Available from: <https://www.mdpi.com/2077-0472/14/7/1156>. Accessed: Oct. 13, 2025.

WENG, L. et al. Unveiling the frontiers of potato disease research through bibliometric analysis. **Frontiers in Microbiology**, v.15, p.1430066, 2024. Available from: <https://www.frontiersin.org/articles/10.3389/fmicb.2024.1430066/full>. Accessed: Oct. 13, 2025.

ZHANG, Z.; ZHU, L. A review on unmanned aerial vehicle remote sensing: platforms, sensors, data processing methods, and applications. **Drones**, v.7, n.6, p.398, 2023. Available from: <https://www.mdpi.com/2504-446X/7/6/398>. Accessed: Aug. 27, 2025.

ZHOU, X. et al. Predicting grain yield in rice using multi-temporal vegetation indices from UAV-based multispectral and digital imagery. **ISPRS Journal of Photogrammetry and Remote Sensing**, v.130, p.246-255, 2017. Available from: <https://linkinghub.elsevier.com/retrieve/pii/S0924271616302337>. Accessed: May, 07, 2025.